

# Polar stratospheric nitric acid depletion surveyed from a decadal dataset of IASI total columns

Gaetane Ronsmans<sup>1,a</sup>, Catherine Wespes<sup>1,a,\*</sup>, Lieven Clarisse<sup>1</sup>, Susan Solomon<sup>2</sup>, Daniel Hurtmans<sup>1</sup>, Cathy Clerbaux<sup>1,3</sup>, and Pierre-François Coheur<sup>1</sup>

<sup>1</sup>Université libre de Bruxelles (ULB), Spectroscopy, Quantum Chemistry and Atmospheric Remote Sensing (SQUARES), Brussels, Belgium

<sup>2</sup>Department of Earth, Atmospheric and Planetary Sciences, Massachusetts Institute of Technology, Cambridge, Massachusetts, USA

<sup>3</sup>LATMOS/IPSL, Sorbonne Université, UVSQ, CNRS, Paris, France

\* Corresponding author: Catherine Wespes (catherine.wespes@ulb.be)

<sup>a</sup> Co-first authors

## Abstract

In this paper, we exploit the first 10-year data-record (2008-2017) of nitric acid ( $\text{HNO}_3$ ) total columns measured by the IASI-A/Metop infrared sounder, characterized by an exceptional daily sampling and a good vertical sensitivity in the lower-to-mid stratosphere (around 50 hPa), to monitor the relationship between the temperature decrease and the observed  $\text{HNO}_3$  loss that occurs each year in the Antarctic stratosphere during the polar night. Since the  $\text{HNO}_3$  depletion results from the formation of polar stratospheric clouds (PSCs) which trigger the development of the ozone ( $\text{O}_3$ ) hole, its continuous monitoring is of high importance. We verify here, from the 10-year time evolution of  $\text{HNO}_3$  together with temperature (taken from reanalysis at 50 hPa), the recurrence of specific regimes in the annual cycle of IASI  $\text{HNO}_3$  and identify, for each year, the day and the 50 hPa temperature ("drop temperature") corresponding to the onset of strong  $\text{HNO}_3$  depletion in the Antarctic winter. Although the measured  $\text{HNO}_3$  total column does not allow the uptake of  $\text{HNO}_3$  by different types of PSC particles along the vertical profile to be differentiated, an average drop temperature of  $194.2 \pm 3.8$  K, close to the nitric acid trihydrate (NAT) existence threshold ( $\sim 195$  K at 50 hPa), is found in the region of potential vorticity lower than  $-10 \times 10^{-5}$  K.m $^2$ .kg $^{-1}$ .s $^{-1}$  (similar to the  $70^\circ - 90^\circ$  S equivalent latitude region during winter). The spatial distribution and inter-annual variability of the drop temperature are investigated and discussed. This paper highlights the capability of the IASI sounder to monitor the evolution of polar stratospheric  $\text{HNO}_3$ , a key player in the processes involved in the depletion of stratospheric  $\text{O}_3$ .

## 1 Introduction

The cold and isolated air masses found within the polar vortex during winter are associated with a strong denitrification of the stratosphere due to the formation of PSCs (composed of  $\text{HNO}_3$ , sulphuric acid ( $\text{H}_2\text{SO}_4$ ) and water ice ( $\text{H}_2\text{O}$ )) (e.g. Peter, 1997; Voigt et al., 2000; von König, 2002; Schreiner et al., 2003; Peter and Groß, 2012). These clouds strongly affect the polar chemistry by (1) acting as surfaces for the heterogeneous activation of chlorine and bromine compounds, in turn leading to enhanced  $\text{O}_3$  destruction (e.g. Solomon, 1999; Wang and Michelangeli, 2006; Harris et al., 2010; Wegner et al., 2012) and by (2) removing gas-phase  $\text{HNO}_3$  temporarily or permanently through uptake by PSCs and sedimentation of large PSC particles to lower altitudes. The denitrification of the polar stratosphere during winter delays the reformation of  $\text{ClONO}_2$ , a chlorine reservoir, and, hence, intensifies the  $\text{O}_3$  hole (e.g. Solomon, 1999; Harris et al., 2010; Tritscher et al., 2021). The heterogeneous reaction rates on PSC surfaces and the uptake of  $\text{HNO}_3$  strongly depend on the temperature and on the PSC particle type. The

49 PSCs are classified into three different types based on their composition and optical properties: type Ia  
50 solid nitric acid trihydrate - NAT ( $\text{HNO}_3 \cdot (\text{H}_2\text{O})_3$ ), type Ib liquid supercooled ternary solution - STS  
51 ( $\text{HNO}_3 / \text{H}_2\text{SO}_4 / \text{H}_2\text{O}$  with variable composition) and type II, crystalline water-ice particles (likely  
52 composed of a combination of different chemical phases) (e.g. Toon et al., 1986; Koop et al., 2000;  
53 Voigt et al., 2000; Lowe and MacKenzie, 2008). In the stratosphere, they mostly consist of mixtures of  
54 liquid/solid STS/NAT particles in varying number densities, with  $\text{HNO}_3$  being the major constituent of  
55 these particles. The large-size NAT particles of low number density are the principal cause of  
56 sedimentation (Lambert et al., 2012; Pitts et al., 2013; Molleker et al., 2014; Lambert et al., 2016). The  
57 formation temperature of STS ( $T_{STS}$ ) and the thermodynamic equilibrium temperatures of NAT ( $T_{NAT}$ )  
58 and ice ( $T_{ice}$ ) have been determined, respectively, as:  $\sim 192$  K (Carslaw et al., 1995),  $\sim 195.7$  K (Hanson  
59 and Mauersberger, 1988) and  $\sim 188$  K (Murphy and Koop, 2005) for typical 50 hPa atmospheric  
60 conditions (5 ppmv  $\text{H}_2\text{O}$  and 10 ppbv  $\text{HNO}_3$ ). While the NAT nucleation was thought to require pre-  
61 existing ice nuclei, hence, temperatures below  $T_{ice}$  (e.g. Zondlo et al., 2000; Voigt et al., 2003), recent  
62 observational and modelling studies have shown that  $\text{HNO}_3$  starts to condense in early PSC season in  
63 liquid NAT mixtures well above  $T_{ice}$  ( $\sim 4$  K below  $T_{NAT}$ , close to  $T_{STS}$ ) even after a very short temperature  
64 threshold exposure (TTE) to these temperatures but also slightly below  $T_{NAT}$  after a long TTE, whereas  
65 the NAT existence persists up to  $T_{NAT}$  (Pitts et al., 2013; Hoyle et al., 2013; Lambert et al., 2016; Pitts  
66 et al., 2018). It has been recently proposed that the higher temperature condensation results from  
67 heterogeneous nucleation of NAT on meteoritic dust in liquid aerosol (Voigt et al., 2005; Hoyle et al.,  
68 2013; Groß et al., 2014; James et al., 2018; Tritscher et al., 2021). Further cooling below  $T_{STS}$  and  $T_{ice}$   
69 leads to nucleation of liquid STS, of solid NAT onto ice and of ice particles mainly from STS (type II  
70 PSCs) (Lowe and MacKenzie, 2008). The formation of NAT and ice has also been shown to be triggered  
71 by stratospheric mountain-waves (Carslaw et al., 1998; Hoffmann et al., 2017). Although the formation  
72 mechanisms and composition of STS droplets in stratospheric conditions are well described (Toon et al.,  
73 1986; Carslaw et al., 1995; Lowe and MacKenzie, 2008), the NAT and ice nucleation processes still  
74 require further investigation (Tritscher et al., 2021). This could be important as the chemistry-climate  
75 models (CCMs) generally oversimplify the heterogeneous nucleation schemes for PSC formation (Zhu  
76 et al., 2015; Spang et al., 2018; Snels et al., 2019), preventing an accurate estimation of  $\text{O}_3$  levels.  
77

78 Over the last few decades, several satellite instruments have measured stratospheric  $\text{HNO}_3$  (e.g.  
79 MLS/UARS (Santee et al., 1999), MLS/Aura (Santee et al., 2007), MIPAS/ENVISAT (Piccolo and  
80 Dudhia, 2007), ACE-FTS/SCISAT (Sheese et al., 2017) and SMR/Odin (Urban et al., 2009)).  
81 Spaceborne instruments such as the CALIOP/CALIPSO lidar and MIPAS/Envisat measuring in the  
82 infrared are capable of detecting and classifying PSC types, allowing their formation mechanisms to be  
83 investigated (Lambert et al., 2016; Pitts et al., 2018; Spang et al., 2018; Tritscher et al., 2021 and  
84 references therein); these satellite data complement in situ measurements (Voigt et al., 2005) and ground-  
85 based lidar (Snels et al., 2019). From these available observational datasets,  $\text{HNO}_3$  depletion has been  
86 linked to PSC formation and detected below the  $T_{NAT}$  threshold (Santee et al., 1999; Urban et al., 2009;  
87 Lambert et al., 2016; Ronsmans et al., 2018), but its relationship to PSCs still needs further investigation  
88 given the complexity of the nucleation mechanisms that depend on several parameters (e.g. atmospheric  
89 temperature, water and  $\text{HNO}_3$  vapour pressure, time exposure to temperatures, temperature history).  
90

91 In contrast to the limb satellite instruments mentioned above, the infrared nadir sounder IASI offers a  
92 dense spatial sampling of the entire globe, twice a day (Section 2). While it cannot provide a vertical  
93 profile of  $\text{HNO}_3$  similar to that from the limb sounders, IASI provides reliable total column  
94 measurements of  $\text{HNO}_3$  characterized by a maximum sensitivity in the low-middle stratosphere around  
95 50 hPa (20 km) during the dark Antarctic winter (Ronsmans et al., 2016, 2018) where PSCs form (Voigt  
96 et al., 2005; Lambert et al., 2012; Spang et al., 2016, 2018). This study aims to explore the 10-year  
97 continuous  $\text{HNO}_3$  measurements from IASI to provide a long-term global picture of depletion and of its

98 dependence on temperatures during polar winter (Section 3). The temperature corresponding to the onset  
99 of the strong depletion in  $\text{HNO}_3$  records (here referred to as ‘drop temperature’) is identified in Section  
100 4 for each observed year and discussed in the context of previous studies.  
101

102 **2 Data**

103

104 The  $\text{HNO}_3$  data used in the present study are obtained from measurements of the Infrared Atmospheric  
105 Sounding Interferometer (IASI) onboard the Metop-A satellite. IASI measures the Earth’s and  
106 atmosphere’s radiation in the thermal infrared spectral range (645 - 2760  $\text{cm}^{-1}$ ), with a 0.5  $\text{cm}^{-1}$  apodized  
107 resolution and a low radiometric noise (Clerbaux et al., 2009; Hilton et al., 2012). Thanks to its polar  
108 sun-synchronous orbit with more than 14 orbits a day and a field of view of four simultaneous footprints  
109 of 12 km at nadir, IASI provides global coverage twice a day (9.30 AM and PM mean local solar time).  
110 That extensive spatial and temporal sampling in the polar regions is key to this study.  
111

112 The  $\text{HNO}_3$  vertical profiles are retrieved on a uniform vertical 1 km grid of 41 layers (from the surface  
113 to 40 km with an extra layer above to 60 km) in near-real-time by the Fast Optimal Retrieval on Layers  
114 for IASI (FORLI) software, using the optimal estimation method (Rodgers, 2000). Detailed information  
115 on the FORLI algorithm and retrieval parameters specific to  $\text{HNO}_3$  can be found in previous papers  
116 (Hurtmans et al., 2012; Ronsmans et al., 2016). For this study, only the total columns (v20151001) are  
117 used, considering (1) the low vertical resolution of IASI with only one independent piece of information  
118 (full width at half maximum - FWHM - of the averaging kernels of  $\sim 30$  km), (2) the limited sensitivity  
119 of IASI to tropospheric  $\text{HNO}_3$ , (3) the dominant contribution of the stratosphere to the  $\text{HNO}_3$  total  
120 column and (4) the largest sensitivity of IASI in the region of interest, i.e. in the low and mid-stratosphere  
121 (from  $\sim 70$  to  $\sim 30$  hPa), where the  $\text{HNO}_3$  abundance is the highest (Ronsmans et al., 2016). The IASI  
122 measurements capture the expected depletion of  $\text{HNO}_3$  within the polar night, as illustrated in Fig. 1 that  
123 shows examples of vertical  $\text{HNO}_3$  profiles retrieved within the dark Antarctic vortex (above Arrival  
124 Heights) and outside the vortex (above Lauder). The retrieved profiles are shown along with their  
125 associated total retrieval error and averaging kernels (the total column averaging kernel and the so-called  
126 “sensitivity profile” are also represented; see Ronsmans et al., 2016 for more details). The total column  
127 averaging kernel (in black) indicates the sensitivity of the total column measurement to changes in the  
128 vertical distribution of  $\text{HNO}_3$ , hence, the altitude to which the retrieved total column is mainly  
129 sensitive/representative, while the sensitivity profile indicates the extent to which the retrieval at one  
130 specific altitude comes from the spectral measurement rather than the a priori. Above Arrival Heights  
131 during the dark Antarctic winter, we clearly see depleted  $\text{HNO}_3$  levels in the low and mid-stratosphere  
132 and the altitude of maximum sensitivity at around 30 hPa for this case (values of  $\sim 1$  along the total  
133 column averaging kernel around that level). In contrast, at Lauder,  $\text{HNO}_3$  levels larger than the a priori  
134 are observed in the stratosphere with a larger range of maximum sensitivity. The total columns are  
135 associated with a total retrieval error ranging from around 3% at mid- and polar latitudes (except above  
136 Antarctica) to 25% above cold Antarctic surface during winter and with a low absolute bias smaller than  
137 12% when compared to ground-based FTIR measurements, in polar regions over the altitude range  
138 where the IASI sensitivity is the largest (see Hurtmans et al., 2012 and Ronsmans et al., 2016 for more  
139 details). The highest error measured over the Antarctic arises from weaker sensitivity above very cold  
140 surface with a degrees of freedom for signal (DOFS) of 0.95 and from a poor knowledge of the seasonally  
141 and wavenumber-dependent emissivity above ice surfaces, which induces larger forward model errors).  
142 In order to expand on the comparisons against FTIR measurements, which cannot be made during the  
143 polar night, Fig. 2 (top panel) presents the time series of daily IASI total  $\text{HNO}_3$  columns co-located with  
144 MLS measurements within  $2.5^\circ \times 2.5^\circ$  grid boxes, averaged in the  $70^\circ\text{S}$ – $90^\circ\text{S}$  equivalent latitude band.  
145 In order to account for the vertical sensitivity of IASI, the averaging kernels associated with each co-  
146 located IASI retrieved profile were applied to the MLS profiles for this cross-comparison. The MLS

147 mixing ratio profiles over the 215-1.5 hPa pressure range were first interpolated to the FORLI pressure  
148 grids and extended down to the surface by using the FORLI-HNO<sub>3</sub> a priori profile, and then converted  
149 into partial columns. Similar variations in the HNO<sub>3</sub> column are captured by the two instruments, with  
150 an excellent agreement in particular for the timing of the strong HNO<sub>3</sub> depletion within the inner vortex  
151 core. Note that a similar good agreement between the two satellite datasets is obtained in other latitude  
152 bands (see Fig. 2 bottom panel for the 50°S–70°S equivalent latitude band; the other bands are not  
153 shown).

154

155 Quality flags similar to those developed for O<sub>3</sub> in previous IASI studies (Wespes et al., 2017) were  
156 applied a posteriori to exclude data (i) with a corresponding poor spectral fit (e.g. based on quality flags  
157 rejecting biased or sloped residuals, fits with maximum number of iteration exceeded), (ii) with less  
158 reliability (e.g. based on quality flags rejecting suspect averaging kernels, data with less sensitivity  
159 characterized by a DOFS lower than 0.9) or (iii) with tropospheric cloud contamination (defined by a  
160 fractional cloud cover  $\geq 25\%$ ). Note that the HNO<sub>3</sub> total column distributions illustrated in sections  
161 below use the median as a statistical average since it is more robust against the outliers than the mean.  
162

163 Temperature and potential vorticity (PV) fields are taken from the ECMWF ERA Interim Reanalysis  
164 dataset, respectively at 50 hPa and at the potential temperature of 530 K (corresponding to  $\sim 20$  km  
165 altitude where the IASI sensitivity to HNO<sub>3</sub> is the highest during the Southern Hemisphere (S.H.) winter  
166 (Ronmans et al., 2016)). Because the HNO<sub>3</sub> uptake by PSCs starts within a few degrees below T<sub>NAT</sub>  
167 ( $\sim 195.7$  K at 50 hPa (Hanson and Mauersberger, 1988)) depending on the meteorological conditions  
168 (Pitts et al., 2013; Hoyle et al., 2013; Lambert et al., 2016; Pitts et al., 2018), a threshold temperature of  
169 195 K is considered in the sections below to identify regions of potential PSC existence. The potential  
170 vorticity is used to delimit dynamically consistent areas in the polar regions. In what follows, we use  
171 either the equivalent latitudes ("eqlat", calculated from PV fields at 530 K) or the PV values to  
172 characterize the relationship between HNO<sub>3</sub> and temperatures in the cold polar regions. Uncertainties in  
173 ERA-Interim temperatures will also be discussed below.  
174

### 175 3 Annual cycle of HNO<sub>3</sub> vs temperatures

176

177 Figure 3a shows the yearly HNO<sub>3</sub> cycle (solid lines, left axis) in the southernmost equivalent latitudes  
178 (70° - 90° S) as measured by IASI over the whole study period (2008–2017). The total HNO<sub>3</sub> variability  
179 in such equivalent latitudes has already been discussed in a previous IASI study (Ronmans et al., 2018),  
180 where the contribution of the PSCs to the HNO<sub>3</sub> variations was highlighted. The temperature time series,  
181 taken at 50 hPa, is represented as well (dashed lines, right axis). From this figure, different regimes of  
182 HNO<sub>3</sub> total columns vs temperature can be observed throughout the year and from one year to another.  
183 In particular, we define here three main regimes (R1, R2 and R3) during the HNO<sub>3</sub>/temperature annual  
184 cycle. The full cycle and the main regimes in the 70° - 90° S eqlat region are further represented in Fig.  
185 3b that shows a histogram of the HNO<sub>3</sub> total columns as a function of temperature for the year 2011.  
186 Similar histograms are observed for the other years in the 10-year study period (not shown). The orange  
187 horizontal and vertical lines in Fig. 3a and Fig. 3b, respectively, represent the 195 K threshold  
188 temperature used to identify the onset of HNO<sub>3</sub> uptake by PSCs (see Section 2). The three regimes  
189 identified are:  
190

- 191 - R1 is defined by the maxima in the total HNO<sub>3</sub> abundances covering the months of April and  
192 May ( $\sim 3 \times 10^{16}$  molec.cm<sup>-2</sup>), when the 50 hPa temperature strongly decreases (from  $\sim 220$  to  $\sim 195$   
193 K). These high HNO<sub>3</sub> levels result from low sunlight, preventing photodissociation, along with  
194 the heterogeneous hydrolysis of N<sub>2</sub>O<sub>5</sub> to HNO<sub>3</sub> during autumn before the formation of polar  
195 stratospheric clouds (Keys et al., 1993; Santee et al., 1999; Urban et al., 2009; de Zafra and

196 Smyshlyaev, 2001). This period also corresponds to the onset of the development of the southern  
197 polar vortex, which is characterized by strong diabatic descent with weak latitudinal mixing  
198 across its boundary, isolating polar  $\text{HNO}_3$ -rich air from lower-latitude airmasses. The end of the  
199 R1 period marks the start of the strong total  $\text{HNO}_3$  decrease that intensifies later in R2.  
200

201 - R2, which extends from June to October, follows the onset of the strong decrease in  $\text{HNO}_3$  total  
202 columns that starts around mid-May in most years when the temperatures fall below 195 K. After  
203 a steep initial decline in total  $\text{HNO}_3$ , R2 is characterized by a plateau of total  $\text{HNO}_3$  minima. For  
204 much of this regime, average  $\text{HNO}_3$  total columns are below  $2 \times 10^{16}$  molec. $\text{cm}^{-2}$  and the 50 hPa  
205 temperatures range mostly between 180 and 190 K.  
206

207 - R3 starts in October when sunlight returns and the 50 hPa temperatures rise above 195 K. Despite  
208 50 hPa temperatures increasing up to 240 K in summer, the  $\text{HNO}_3$  total columns stagnate at the  
209 R2 plateau levels (around  $1.5 \times 10^{16}$  molec. $\text{cm}^{-2}$ ). This regime likely reflects the photolysis of  $\text{NO}_3$   
210 and  $\text{HNO}_3$  itself (Ronmans et al., 2018) as well as the permanent denitrification of the mid-  
211 stratosphere, caused by sedimentation of PSCs. The likely renitrification of the lowermost  
212 stratosphere (e.g. Braun et al., 2019; Lambert et al., 2012), where the  $\text{HNO}_3$  concentrations and  
213 the IASI sensitivity to  $\text{HNO}_3$  are lower (Ronmans et al., 2016), cannot be inferred from the IASI  
214 total column measurements. The plateau lasts until approximately February, when  $\text{HNO}_3$  total  
215 column slowly starts increasing, reaching the April-May maximum in R1.  
216

217 As illustrated in Fig. 3a, the three regimes are observed each year with, however, some interannual  
218 variations. For instance, the sudden stratospheric warming (SSW) that occurred in 2010 (see the  
219 temperature time series at 20 hPa for the year 2010; green dotted line) yielded higher  $\text{HNO}_3$  total columns  
220 (see green solid line in July - September) (de Laat and van Weele, 2011; Klekociuk et al., 2011; WMO,  
221 2014; Ronmans et al., 2018).

222 Figure 3c shows the evolution of the relationship between the daily averaged  $\text{HNO}_3$  (calculated from a  
223 7-day moving average) with the highest occurrence (in bins of  $0.1 \times 10^{16}$  molec. $\text{cm}^{-2}$  and of 2K) and the  
224 50 hPa temperature, over the 10-year study period. The red vertical line represents the 195 K threshold  
225 temperature. Figure 3c also highlights a large interannual variability in total  $\text{HNO}_3$  in R3, while the  
226 strong depletion in  $\text{HNO}_3$  in R2 is consistent every year. Given that PSC formation spans a large range  
227 of altitudes (typically between 10 and 30 km) (Höpfner et al., 2006, 2009; Spang et al., 2018; Pitts et al.,  
228 2018) and that IASI has maximum sensitivity to  $\text{HNO}_3$  around 50 hPa (Hurtmans et al., 2012; Ronmans  
229 et al., 2016), the temperatures at two other pressure levels, namely 70 and 30 hPa (i.e.  $\sim 15$  and  $\sim 25$  km),  
230 have also been tested to investigate the relationship between  $\text{HNO}_3$  and temperature in the low and mid-  
231 stratosphere. The results (not shown here) exhibit a similar  $\text{HNO}_3$ -temperature behavior at the different  
232 levels with, as expected, lower and higher temperatures in R2, respectively, at 30 hPa and at 70 hPa  
233 (temperatures down to  $\sim 180$  K at 30 hPa and down to  $\sim 185$  K at 70 hPa, as compared to temperatures  
234 down to  $\sim 182$  K at 50 hPa, are observed), but still below the NAT formation threshold at these pressure  
235 levels ( $T_{\text{NAT}} \sim 193$  K at 30 hPa and  $\sim 197$  K at 70 hPa) (Lambert et al., 2016). Therefore, the altitude range  
236 of maximum IASI sensitivity to  $\text{HNO}_3$  (see Section 2) is characterized by temperatures that are below  
237 the NAT formation threshold at these pressure levels, enabling PSC formation and the denitrification  
238 process. Furthermore, the consistency between the 195 K threshold temperature taken at 50 hPa and the  
239 onset of the strong total  $\text{HNO}_3$  depletion seen in IASI data (see Fig. 3a) is in agreement with the largest  
240 NAT area that starts to develop in June around 20 km (Spang et al., 2018), which justifies the use of the  
241 195 K temperature at that single representative level in this study.  
242

#### 244 4 Onset of $\text{HNO}_3$ depletion and drop temperature detection

245 To identify the spatial and temporal variability of the onset of the depletion phase, the daily time  
246 evolution of  $\text{HNO}_3$  during the first 10 years of IASI measurements and the temperatures at 50 hPa are  
247 explored. In particular, the second derivative of  $\text{HNO}_3$  total column with respect to time is calculated to  
248 detect the strongest rate of decrease seen in the  $\text{HNO}_3$  time series and to identify its associated day and  
249 50 hPa temperature.

250

#### 251 **4.1 $\text{HNO}_3$ vs temperature time series**

252

253 Figure 4 shows the time series of the second derivative of  $\text{HNO}_3$  total column with respect to time (blue)  
254 and of the temperature (red) averaged in the area of potential vorticity smaller than  $-10 \times 10^{-5} \text{ K} \cdot \text{m}^2 \cdot \text{kg}^{-1} \cdot \text{s}^{-1}$   
255 at the potential temperature of 530 K to encompass the region inside the inner polar vortex where  
256 the temperatures are the coldest and the largest depletion of total  $\text{HNO}_3$  occurs (Ronsmans et al., 2018).  
257 The use of that PV threshold value explains the gaps in the time series during the summer when the PV  
258 does not reach such low levels, while the time series averaged in the  $70^\circ$ -  $90^\circ$  S eqlat band (dashed blue  
259 for the second derivative of  $\text{HNO}_3$  and grey for the temperature) covers the full year. Note that the  $\text{HNO}_3$   
260 time series has been smoothed with a simple spline data interpolation function to avoid gaps in order to  
261 calculate the second derivative of  $\text{HNO}_3$  total column with respect to time as the daily second-difference  
262 in  $\text{HNO}_3$  total columns. The horizontal red line shows the 195 K threshold.

263

264 As already illustrated in Fig. 3a and Fig. 3c, the strongest rate of  $\text{HNO}_3$  depletion (i.e. the second  
265 derivative minimum) is found around the time that temperatures drop below the 195 K threshold (at  
266 exactly or a few days after the detection of the 195 K threshold temperature, particularly for the year  
267 2009), within a few days to a few weeks (4 to 23 days) after total  $\text{HNO}_3$  reaches its maximum, i.e.  
268 between the 11th of May (2013) and the 8th of June (2009). The 50 hPa drop temperatures, i.e. the  
269 temperature associated with the strongest rate of  $\text{HNO}_3$  depletion detected from IASI, are between 189.2  
270 K and 198.6 K, with the exception of the year 2014, which shows a drop temperature of 202.8 K. On  
271 average over the 10 years of studied IASI measurements, a 50 hPa drop temperature of  $194.2 \text{ K} \pm 3.8 \text{ K}$   
272 ( $1\sigma$  standard deviation) is found. Knowing that  $T_{\text{NAT}}$  can be higher or lower depending on the  
273 atmospheric conditions and that NAT starts to nucleate from  $\sim 2$ – $4$  K below  $T_{\text{NAT}}$  (Pitts et al., 2011;  
274 Hoyle et al., 2013; Lambert et al., 2016), the results here tend to demonstrate the consistency between  
275 the 50 hPa drop temperature and the PSC existence temperature in that altitude region. Note that the  
276 range observed in the 50 hPa drop temperature could reflect variations in the preponderance of one type  
277 of PSCs over another from one year to the next. The results further justify the use of the single 50 hPa  
278 level for characterizing and investigating the onset of  $\text{HNO}_3$  depletion from IASI. Nevertheless, given  
279 the range of maximum IASI sensitivity to  $\text{HNO}_3$  around 50 hPa, typically between 70 and 30 hPa  
280 (Ronsmans et al., 2016), the drop temperatures are also calculated at these two other pressure levels (not  
281 shown here) in order to estimate the uncertainty of the calculated drop temperature defined in this study  
282 at 50 hPa. The 30 hPa and 70 hPa drop temperatures range respectively over 185.7 K – 194.9 K and over  
283 194.8 K – 203.7 K, with an average of  $192.0 \pm 2.9 \text{ K}$  and  $198.0 \pm 3.2 \text{ K}$  ( $1\sigma$  standard deviation) over the  
284 ten years of IASI. The average values at 30 hPa and 70 hPa fall within the  $1\sigma$  standard deviation  
285 associated with the average drop temperature at 50 hPa. It is also worth noting the agreement between  
286 the drop temperatures and the NAT formation threshold at these two pressure levels ( $T_{\text{NAT}} \sim 193 \text{ K}$  at 30  
287 hPa and  $\sim 197 \text{ K}$  at 70 hPa) (Lambert et al., 2016). Finally, it should be noted that, because the size, shape  
288 or location of the vortex vary slightly over the altitude range to which IASI is sensitive (from  $\sim 30$  to  $\sim 70$   
289 hPa during the polar night), the use of a single potential temperature surface for the calculation of drop  
290 temperatures could introduce some uncertainties into the results. However, several tests suggest that  
291 these variations of the vortex are overall minor and, hence, have only limited influence on the

292

293 identification of the inner polar vortex (delimited by a PV value of  $-10 \times 10^{-5} \text{ K} \cdot \text{m}^2 \cdot \text{kg}^{-1} \cdot \text{s}^{-1}$  at 530 K) and  
294 on the determination of the average drop temperature inside that region.

295  
296 Figures 5a and b show the climatological zonal distribution of  $\text{HNO}_3$  total columns and of the  
297 temperature at 50 hPa, respectively, spanning the  $55^\circ \text{S}$  -  $90^\circ \text{S}$  geographic latitude band over the first  
298 ten years of IASI, with, superimposed, three isocontour levels of potential vorticity (-10, -8 and  $-5 \times 10^{-5}$   
299  $\text{K} \cdot \text{m}^2 \cdot \text{kg}^{-1} \cdot \text{s}^{-1}$  in blue, cyan and black, respectively) and the isocontours for the 195 K temperature (pink)  
300 and for the averaged 194.2 K drop temperature (purple) at 50 hPa. They further illustrate the relationship  
301 between the IASI total  $\text{HNO}_3$  columns and the 50 hPa temperatures. The climatological (2008-2017) PV  
302 isocontour of  $-10 \times 10^{-5} \text{ K} \cdot \text{m}^2 \cdot \text{kg}^{-1} \cdot \text{s}^{-1}$  is clearly shown to separate well the region of strong depletion in  
303 total  $\text{HNO}_3$ , according to the latitude and the time, until October. The red vertical dashed line indicates  
304 the annual average of the dates on which the 50 hPa drop temperatures are calculated in the area of  $\text{PV} \leq$   
305  $-10 \times 10^{-5} \text{ K} \cdot \text{m}^2 \cdot \text{kg}^{-1} \cdot \text{s}^{-1}$  ( $194.2 \pm 3.8 \text{ K}$ ; see Fig. 4) over the first ten years of IASI. It shows that the  
306 strongest rate of  $\text{HNO}_3$  depletion occurs on average at the end of May (24 May), a few days after the  
307 temperature decreases below 195 K. The yearly zonally averaged time series over the 10-year study  
308 period can be found in Fig. 6, which shows that IASI measures similar  $\text{HNO}_3$  total column zonal  
309 distributions every year, in particular with respect to the edge of the collar region and of the region of  
310 strong depletion (respectively delimited by the PV isocontours of  $-5 \times 10^{-5} \text{ K} \cdot \text{m}^2 \cdot \text{kg}^{-1} \cdot \text{s}^{-1}$  and of  $-10 \times 10^{-5}$   
311  $\text{K} \cdot \text{m}^2 \cdot \text{kg}^{-1} \cdot \text{s}^{-1}$  at 530 K). An exact timing or a delay of a few days between the detection of the averaged  
312 195 K threshold temperature and the start of the  $\text{HNO}_3$  depletion is visible every year in Fig. 6. In  
313 particular, the year 2009 shows the longest delay (see also Fig. 4). Note that the mismatch observed in  
314 the 10-year average between the detection of the averaged 195 K threshold temperature and the average  
315 date for the drop temperatures (see Fig. 5 a and b) is driven by the year 2013 which is characterized by  
316 the lowest temperatures during the Antarctic winter over the 10-year study period and, hence, the earliest  
317 date for the drop temperature (11th of May; see Fig. 4 and Fig. 6).

## 320 **4.2 Spatial distribution of drop temperatures**

321  
322 To explore the capability of IASI to monitor the onset of  $\text{HNO}_3$  depletion at a large scale, figure 7 shows,  
323 for each year of the study period, the spatial distribution of the 50 hPa drop temperatures based on the  
324 second derivative minima of total  $\text{HNO}_3$  averaged in  $1^\circ \times 1^\circ$  grid cells. The region of interest here is  
325 delimited by a PV value of  $-8 \times 10^{-5} \text{ K} \cdot \text{m}^2 \cdot \text{kg}^{-1} \cdot \text{s}^{-1}$  at 530 K, in order to investigate an area a bit larger  
326 than the inner vortex core that was the focus of the preceding discussion (delineated in green in figure 7  
327 by the PV isocontour of  $-10 \times 10^{-5} \text{ K} \cdot \text{m}^2 \cdot \text{kg}^{-1} \cdot \text{s}^{-1}$  averaged over the interval 10 May to 15 July). The  
328 isocontour of  $-10 \times 10^{-5} \text{ K} \cdot \text{m}^2 \cdot \text{kg}^{-1} \cdot \text{s}^{-1}$  for the minimum PV (in cyan) encountered at 530 K over the 10  
329 May to 15 July period for each year, as well as the isocontours of 195 K for the average temperatures  
330 and the minimum temperatures, are also represented. The calculated drop temperatures corresponding  
331 to the onset of  $\text{HNO}_3$  depletion inside the averaged PV isocontour are found to vary between  $\sim 180$  and  
332  $\sim 210 \text{ K}$  and the corresponding dates range between  $\sim$ mid-May and mid-July (not shown here). Although  
333 the range of drop temperatures and dates for  $1^\circ \times 1^\circ$  bins is broader than that found for the inner vortex  
334 averages discussed above, the results are qualitatively consistent. For example, the year 2014 that shows  
335 the highest inner vortex average drop temperature in Figure 4 is characterized by the highest drop  
336 temperatures above the eastern Antarctic. Note, however, that the high extremes in the drop temperature,  
337 mainly found above the eastern Antarctic, should be considered with caution: they correspond to specific  
338 regions above ice surfaces with emissivity features that are known to yield errors in the IASI retrievals  
339 (Hurtmans et al., 2012; Ronsmans et al., 2016). Indeed, bright land surfaces such as ice might in some  
340 cases lead to poor  $\text{HNO}_3$  retrievals. Although wavenumber-dependent surface emissivity atlases are used  
341 in FORLI (Hurtmans et al., 2012), this parameter remains critical and causes poorer retrievals that, in

342 some instances, pass through the series of quality filters and could affect the drop temperature  
343 calculation.

344  
345 The averaged isocontour of 195 K encircles fairly well the area of  $\text{HNO}_3$  drop temperatures lower than  
346 195 K (typically from  $\sim 187$  K to  $\sim 195$  K), which means that the bins inside that area include airmasses  
347 that experience the NAT threshold temperature during a long time over the 10 May – 15 July period.  
348 That area encompasses the inner vortex core (delimited by the isocontour of  $-10 \times 10^{-5} \text{ K.m}^2.\text{kg}^{-1}.\text{s}^{-1}$  for  
349 the PV averaged over the 10 May – 15 July period) and shows pronounced minima (lower than  $-0.5 \times 10^{14}$   
350  $\text{molec.cm}^{-2}.\text{d}^{-2}$ ) in the second derivative of the  $\text{HNO}_3$  total column with respect to time (not shown here),  
351 which indicate a strong and rapid  $\text{HNO}_3$  depletion. The area enclosed between the two isocontours of  
352 195 K for the temperatures, the averaged one and the one for the minimum temperatures, shows generally  
353 higher drop temperatures and weakest minima (larger than  $-0.5 \times 10^{14} \text{ molec.cm}^{-2}.\text{d}^{-2}$ ) in the second  
354 derivative of the  $\text{HNO}_3$  total column (not shown). That area is also typically enclosed by the isocontour  
355 of  $-10 \times 10^{-5} \text{ K.m}^2.\text{kg}^{-1}.\text{s}^{-1}$  for the minimum PV, meaning that the bins inside correspond, at least for one  
356 day over the 10 May – 15 July period, to airmasses located at the inner edge of the vortex and  
357 characterized by temperature lower than the NAT threshold temperature. The fact that the weakest  
358 minima in the second derivative of total  $\text{HNO}_3$  are observed in that area (not shown) indicates a weak  
359 and slow  $\text{HNO}_3$  depletion that might be explained by air masses at the inner edge of the vortex  
360 experiencing only a short period with temperatures below the NAT threshold temperature. It could also  
361 reflect mixing with strongly  $\text{HNO}_3$ -depleted and colder airmasses from the inner vortex core. Mixing  
362 with these already depleted airmasses could also explain the higher drop temperatures detected in those  
363 bins. These sometimes unrealistic high drop temperatures are generally detected later (after the strong  
364  $\text{HNO}_3$  depletion occurs in the inner vortex core, i.e. after the 10 May – 15 July period considered here –  
365 not shown), which supports the transport, in those bins, of previously  $\text{HNO}_3$ -depleted airmasses and the  
366 likely mixing at the edge of the vortex. Note, however, that previous studies have shown a generally  
367 weak mixing in the Antarctic between the edge region and the vortex core (e.g. Roscoe et al., 2012).  
368 Finally, these spatial variations might also partly reflect some uncertainty in the drop temperature  
369 calculation, introduced by the use of temperature at a single pressure level (50 hPa) and of PV on a single  
370 potential temperature surface (530 K) while the sensitivity of IASI to changes in the  $\text{HNO}_3$  profiles  
371 extends over a range from  $\sim 30$  to  $\sim 70$  hPa during the polar night. It should be noted that biases in the  
372 ECMWF ERA Interim temperatures used in this work are too small to explain the large range of drop  
373 temperatures calculated here. Indeed, Lambert and Santee (2018) found only a small warm bias, with  
374 median differences around 0.5 K, reaching 0–0.25 K in the southernmost regions of the globe at  $\sim 68$ – $21$   
375 hPa where PSCs form, through comparisons with the Constellation Observing System for Meteorology,  
376 Ionosphere and Climate (COSMIC) data.  
377

378 Except above some parts of Antarctica which are prone to larger retrieval errors and where unrealistic  
379 high drop temperatures are found, the overall range in the 50 hPa drop temperature for total  $\text{HNO}_3$  inside  
380 the isocontour for the averaged temperature of 195 K typically extends from  $\sim 187$  K to  $\sim 195$  K, which  
381 falls within the range of PSC nucleation temperature at 50 hPa: from slightly below  $T_{\text{NAT}}$  to around 3–4  
382 K below the ice frost point -  $T_{\text{ice}}$  - depending on atmospheric conditions, on TTE and on the specific  
383 formation mechanism (i.e., the type of PSC developing) (Pitts et al., 2011; Peter and Groß, 2012; Hoyle  
384 et al., 2013). This underlines well the benefit of the excellent spatial and temporal coverage of IASI,  
385 which allows the rapid and critical depletion phase to be captured in detail over a large scale.

386  
387 **5 Conclusions**  
388

389 In this paper, we have explored the added value of the dense  $\text{HNO}_3$  total column dataset provided by the  
390 IASI/Metop-A satellite over a full decade (2008–2017) for monitoring the stratospheric depletion phase

391 that occurs each year in the S.H. and for investigating its relationship to the NAT formation temperature.  
392 To that end, we focused on and delimited the coldest polar region of the S.H. using a specific PV value  
393 at 530 K ( $\sim 50$  hPa, PV of  $-10 \times 10^{-5}$  K.m $^2$ .kg $^{-1}$ .s $^{-1}$ ) and stratospheric temperatures at 50 hPa, taken from  
394 the ECMWF ERA Interim reanalysis. That single representative pressure level has been considered in  
395 this study given the maximum sensitivity of IASI to HNO $_3$  around that level, which lies in the range  
396 where the PSCs formation/denitrification processes occur.  
397

398 The annual cycle of total HNO $_3$ , as observed from IASI, has first been characterized according to the  
399 temperature evolution. Three regimes (R1 to R3) in the total HNO $_3$  - 50 hPa temperature relationship  
400 were highlighted from the time series over the S.H. polar region: R1 is defined during April and May  
401 and characterized by a rapid decrease in 50 hPa temperatures while HNO $_3$  accumulates over the pole;  
402 R2, from June to October, follows the onset of the depletion that starts around mid-May in most years  
403 when the 50 hPa temperatures fall below 195 K (considered here as the onset of PSC nucleation phase  
404 at that level), with a strong consistency from year to year; R3, defined from October through March  
405 when total HNO $_3$  remains at low R2 plateau levels, despite the return of sunlight and heat, characterizes  
406 the strong denitrification of the stratosphere, likely due to PSC sedimentation to lower levels where the  
407 IASI sensitivity is low. For each year over the 10-year study period, the use of the second derivative of  
408 the HNO $_3$  column versus time was then found to be particularly valuable to detect the onset of the HNO $_3$   
409 condensation into PSCs. It is captured, on average from IASI, a few days before June with a delay of 4–  
410 23 days after the maximum in total HNO $_3$ . The corresponding temperatures ('drop temperatures') were  
411 detected between 189.2 K and 202.8 K ( $194.2 \pm 3.8$  K on average over the 10 years), which tends to  
412 demonstrate the good consistency between the 50 hPa drop temperature and the PSC formation  
413 temperatures in that altitude region. Finally, the annual and spatial variability (within  $1^\circ \times 1^\circ$ ) in the drop  
414 temperature was further explored from IASI total HNO $_3$ . Inside the isocontours of 195 K for the average  
415 temperatures and of  $-10 \times 10^{-5}$  K.m $^2$ .kg $^{-1}$ .s $^{-1}$  for the averaged PV at 530 K, the drop temperatures are  
416 detected between  $\sim$ mid-May and mid-July, typically range between  $\sim$ 187 K to  $\sim$ 195 K and are associated  
417 with the lowest minima (lower than  $-0.5 \times 10^{14}$  molec.cm $^{-2}$ .d $^{-2}$ ) in the second derivative of the HNO $_3$  total  
418 column with respect to time, indicating a strong and rapid HNO $_3$  depletion. Except for unrealistic drop  
419 temperatures ( $\sim$ 210 K) that were found in some years above eastern Antarctica and suspected to result  
420 from unfiltered poor quality retrievals arising from emissivity issues above ice, the range of drop  
421 temperatures is interestingly found to be in line with the PSC nucleation temperature that is known, from  
422 previous studies, to strongly depend on several factors (e.g. meteorological conditions, HNO $_3$  vapour  
423 pressure, temperature threshold exposure, presence of meteoritic dust). At the edge of the vortex,  
424 considering the isocontours of 195 K for the minimum temperatures or of  $-10 \times 10^{-5}$  K.m $^2$ .kg $^{-1}$ .s $^{-1}$  for the  
425 minimum PV, higher and later drop temperatures along with weakest minima in the second derivative  
426 of the HNO $_3$  total column with respect to time, indicating a slow HNO $_3$  depletion, are found. These  
427 likely result from a short temperature threshold exposure or mixing with already depleted airmasses from  
428 the inner vortex core. The results of this study highlight the ability of IASI to measure the variations in  
429 total HNO $_3$  and, in particular, to capture and monitor the rapid depletion phase over the whole Antarctic  
430 region.  
431

432 We show in this study that the IASI dataset allows the variability of stratospheric HNO $_3$  throughout the  
433 year (including the polar night) in the Antarctic to be captured. In that respect, it offers observational  
434 means to monitor the relation of HNO $_3$  to temperature and the related formation of PSCs. Despite the  
435 limited vertical resolution of IASI which does not allow investigation of the HNO $_3$  uptake by the  
436 different types of PSCs during their formation and growth along the vertical profile, the HNO $_3$  total  
437 column measurements from IASI constitute an important new dataset for exploring the strong polar  
438 depletion over the whole stratosphere. This is particularly relevant considering the mission continuity,  
439 which will span several decades with the planned follow-on missions. Indeed, thanks to the three

440 successive instruments (IASI-A launched in 2006 and still operating, IASI-B in 2012, and IASI-C in  
441 2018) that demonstrate an excellent stability of the Level-1 radiances, the measurements will soon  
442 provide an unprecedented long-term dataset of  $\text{HNO}_3$  total columns. Further work could also make use  
443 of this unique data set to investigate the relation between  $\text{HNO}_3$ ,  $\text{O}_3$ , and meteorology in the changing  
444 climate.

445

446

#### 447 **Data availability**

448 The IASI  $\text{HNO}_3$  data processed with FORLI- $\text{HNO}_3$  v0151001 are available upon request to the  
449 corresponding author.

450

#### 451 **Author contributions**

452 C.W. and G.R. performed the analysis, wrote the manuscript and prepared the figures. L.C. contributed  
453 to the analysis. S.S., P.-F. C. and L.C. contributed to the interpretation of the results. D.H. was  
454 responsible for the retrieval algorithm development and the processing of the IASI  $\text{HNO}_3$  dataset. All  
455 authors contributed to the writing of the text and reviewed the manuscript.

456

#### 457 **Competing interests**

458 The authors declare no competing interests.

459

#### 460 **Acknowledgements**

461 IASI has been developed and built under the responsibility of the Centre National d'Etudes Spatiales  
462 (CNES, France). It is flown on board the Metop satellites as part of the EUMETSAT Polar System. The  
463 IASI L1 data are received through the EUMETCast near-real-time data distribution service. The research  
464 was funded by the F.R.S.-FNRS, the Belgian State Federal Office for Scientific, Technical and Cultural  
465 Affairs (Prodex arrangement 4000111403 IASI.FLOW) and EUMETSAT through the Satellite  
466 Application Facility on Atmospheric Composition Monitoring (ACSAF). G. Ronsmans is grateful to the  
467 Fonds pour la Formation à la Recherche dans l'Industrie et dans l'Agriculture of Belgium for a PhD  
468 grant (Boursier FRIA). L. Clarisse is a research associate supported by the F.R.S.-FNRS. C. Clerbaux is  
469 grateful to CNES for financial support. S. Solomon is supported by the National Science Foundation  
470 (NSF-1539972). We also would like to thank the three reviewers for their helpful comments and  
471 corrections and, in particular, M. Santee for her in-depth reviews, which have substantially improved  
472 the paper quality.

473

474

475

476

477

478

479

480

481

482

483

484

485

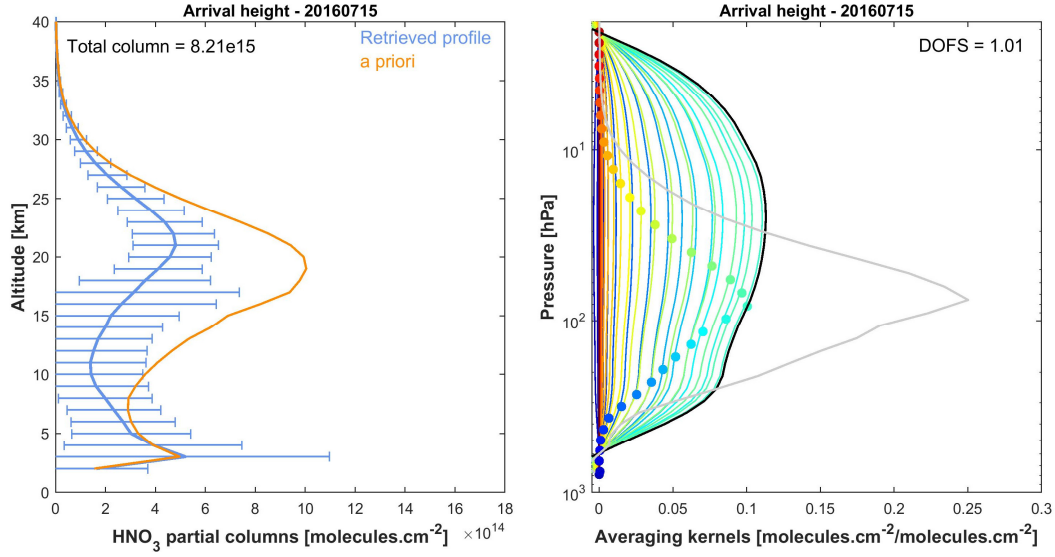
486

487

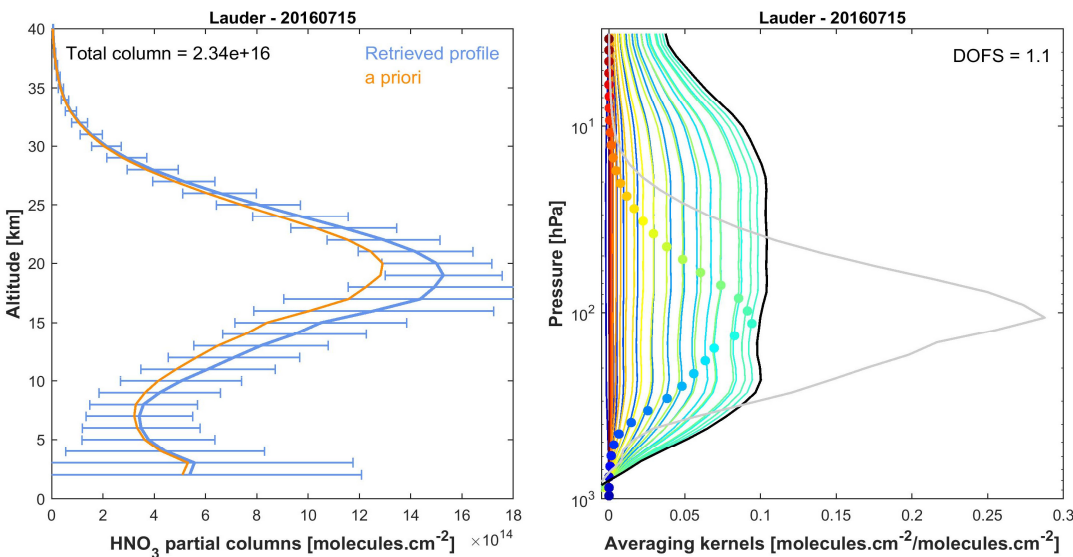
488

489  
490  
491  
492

## Figure captions

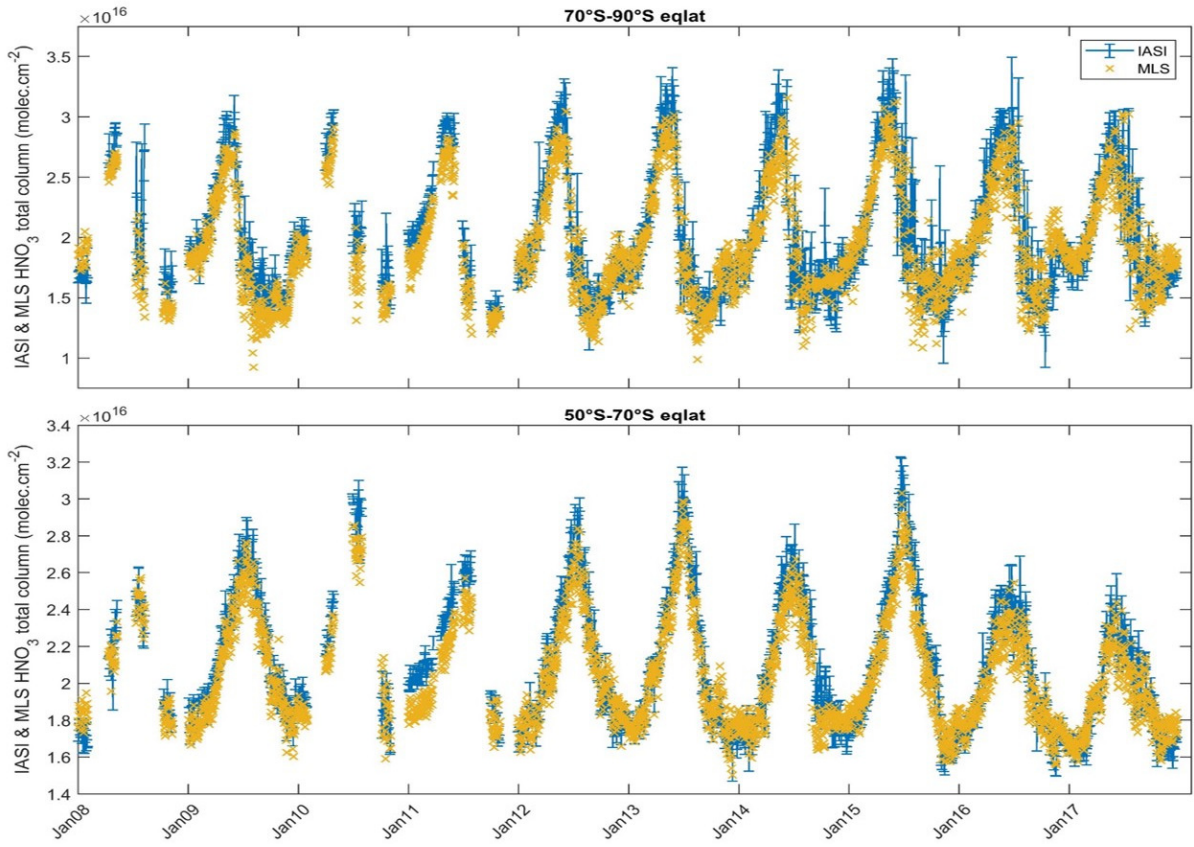


494

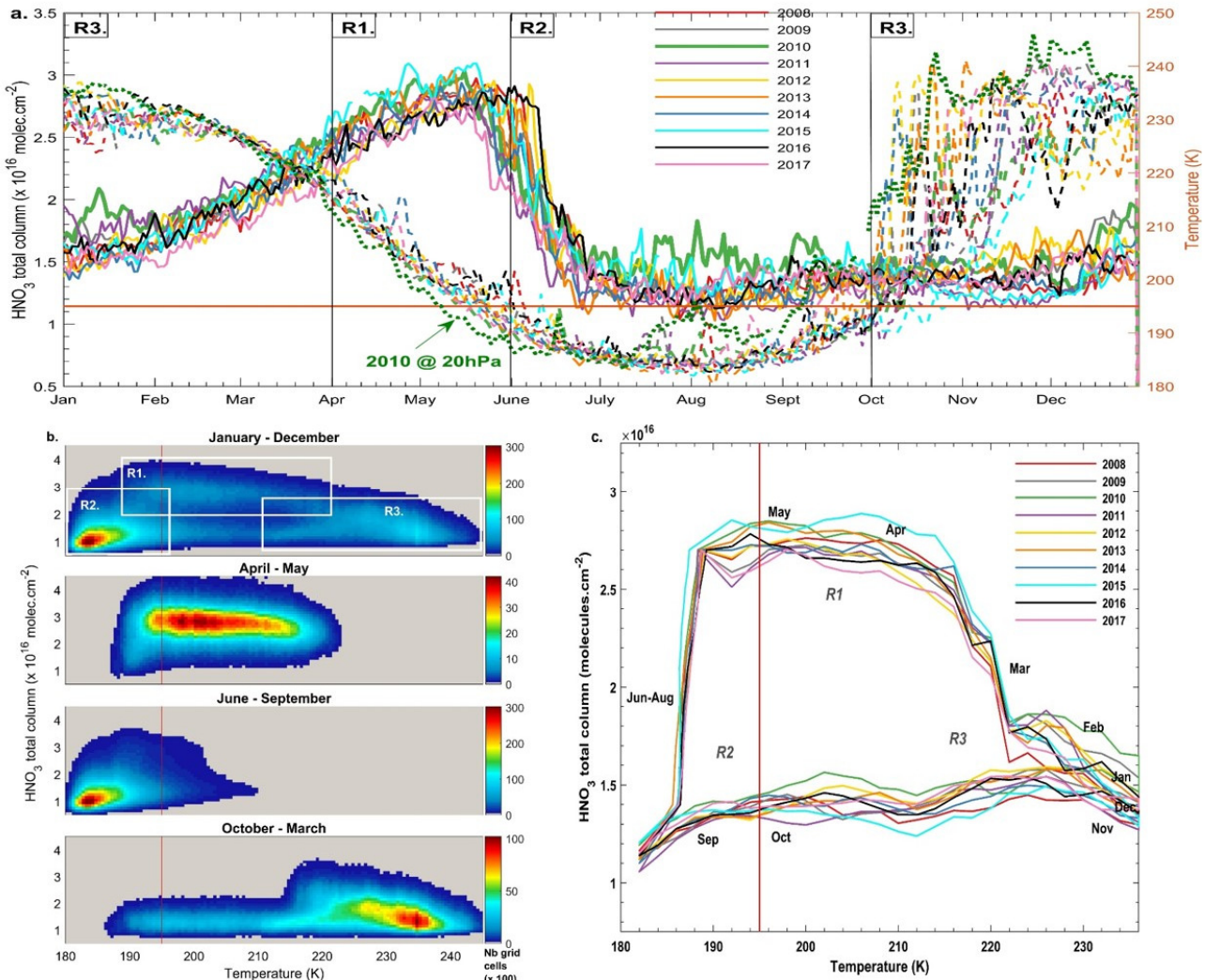


495  
496  
497  
498  
499  
500  
501  
502  
503

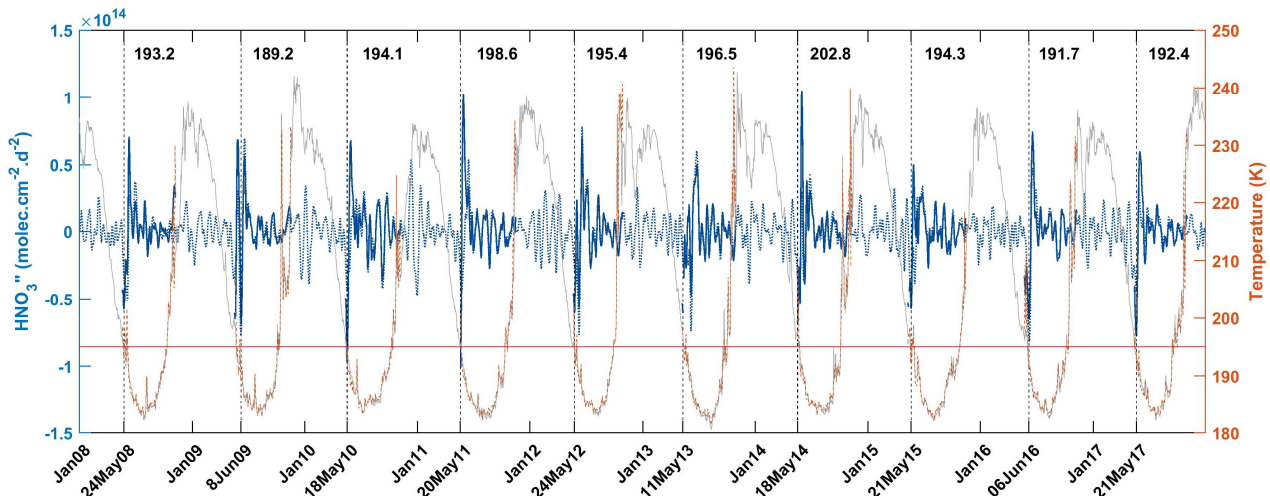
Figure 1. Examples of IASI  $\text{HNO}_3$  vertical profiles (in  $\text{molec.cm}^{-2}$ ) with corresponding averaging kernels (in  $\text{molec.cm}^{-2}/\text{molec.cm}^{-2}$ ; colored lines, with the altitude of each kernel represented by the colored dots) along with the total column averaging kernels (black) and the sensitivity profiles (grey) (both divided by 10) above Arrival Heights ( $77.49^\circ\text{S}$ ,  $166.39^\circ\text{E}$ , top panels) and Lauder ( $45.03^\circ\text{S}$ ,  $169.40^\circ\text{E}$ ; bottom panels). The error bars associated with the  $\text{HNO}_3$  vertical profile represent the total retrieval error. The a priori profile is also represented. The total column and the DOFS values are indicated.



504  
505  
506 **Figure 2.** Time series of daily IASI total  $\text{HNO}_3$  column (blue) co-located with MLS and of MLS total  $\text{HNO}_3$   
507 columns (orange) within  $2.5^\circ \times 2.5^\circ$  grid boxes, averaged in the  $70^\circ\text{S}$ – $90^\circ\text{S}$  (top panel) and the  $50^\circ\text{S}$ – $70^\circ\text{S}$  (bottom panel)  
508 equivalent latitude bands. Note that the MLS total column estimates were obtained by extending the  
509 MLS partial stratospheric column values using the FORLI- $\text{HNO}_3$  a priori information (see text for  
510 details). The error bars (blue) represent  $3\sigma$ , where  $\sigma$  is the standard deviation around the IASI  $\text{HNO}_3$  daily  
511 average.



520  
 521  
 522 **Figure 3.** (a) Time series of daily averaged HNO<sub>3</sub> total columns (solid lines) and temperatures taken at 50 hPa  
 523 (dashed lines) in the 70° - 90° S equivalent latitude band, for the years 2008 – 2017. The green dotted line  
 524 represents the temperatures at 20 hPa for the year 2010. (b) HNO<sub>3</sub> total columns versus temperatures (at 50 hPa)  
 525 histogram during the year 2011, over the whole year (top) and for the 3 defined regimes (R1 - R3) separated in  
 526 (a). The colors refer to the number of gridded measurements in each cell. (c) Evolution of daily averaged HNO<sub>3</sub>  
 527 total columns with the highest occurrence (in bins of  $0.1 \times 10^{16}$  molec.cm<sup>-2</sup> and 2 K) as a function of the 50 hPa  
 528 temperature for the years 2008 – 2017. The orange horizontal or vertical lines represent the 195 K threshold  
 529 temperature.



538  
539

540 **Figure 4.** Time series of total  $\text{HNO}_3$  second derivative (blue, left y-axis) and of the 50 hPa temperature (red, right y-axis), in the region of potential vorticity at 530 K lower than  $-10 \times 10^{-5} \text{ K.m}^2\text{.kg}^{-1}\text{.s}^{-1}$ . The red horizontal line  
541 corresponds to the 195 K temperature. The vertical dashed lines indicate the second derivative minimum in  $\text{HNO}_3$   
542 for each year. The corresponding dates (in bold, on the x-axis) and temperatures are also indicated. The time series  
543 of total  $\text{HNO}_3$  second derivative (dashed blue) and of temperature (grey) in the  $70^\circ - 90^\circ \text{S}$  eqlat band are also  
544 represented.  
545

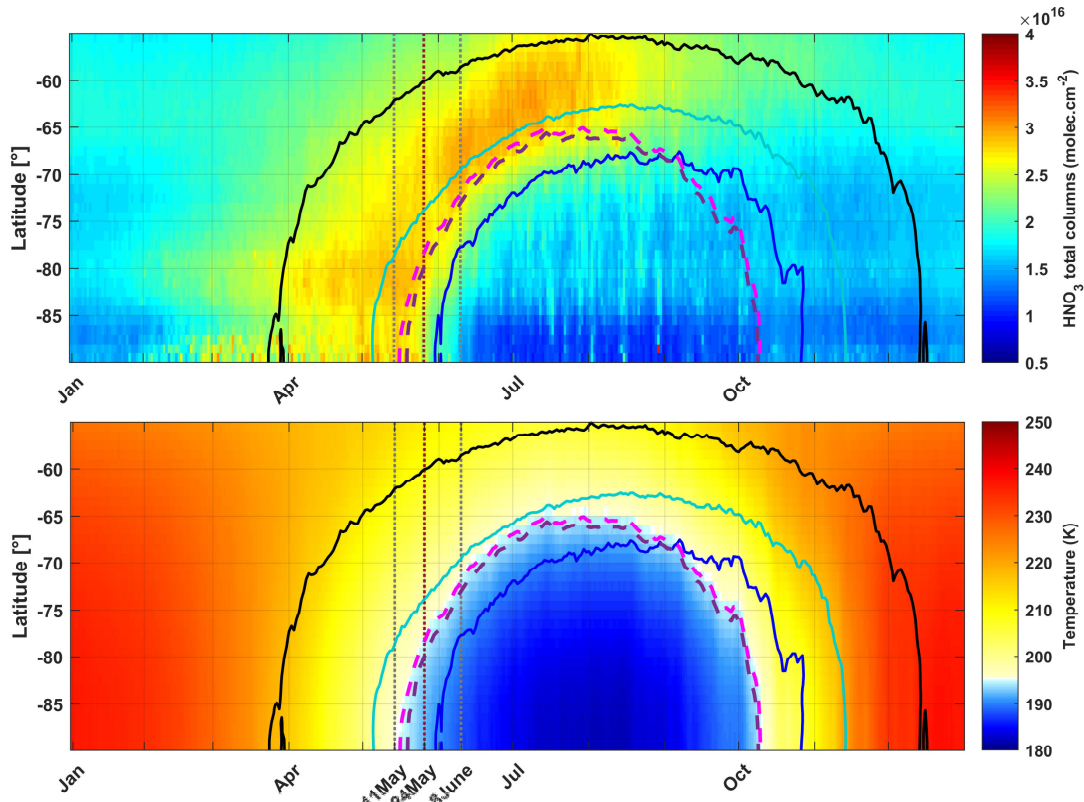
546

547

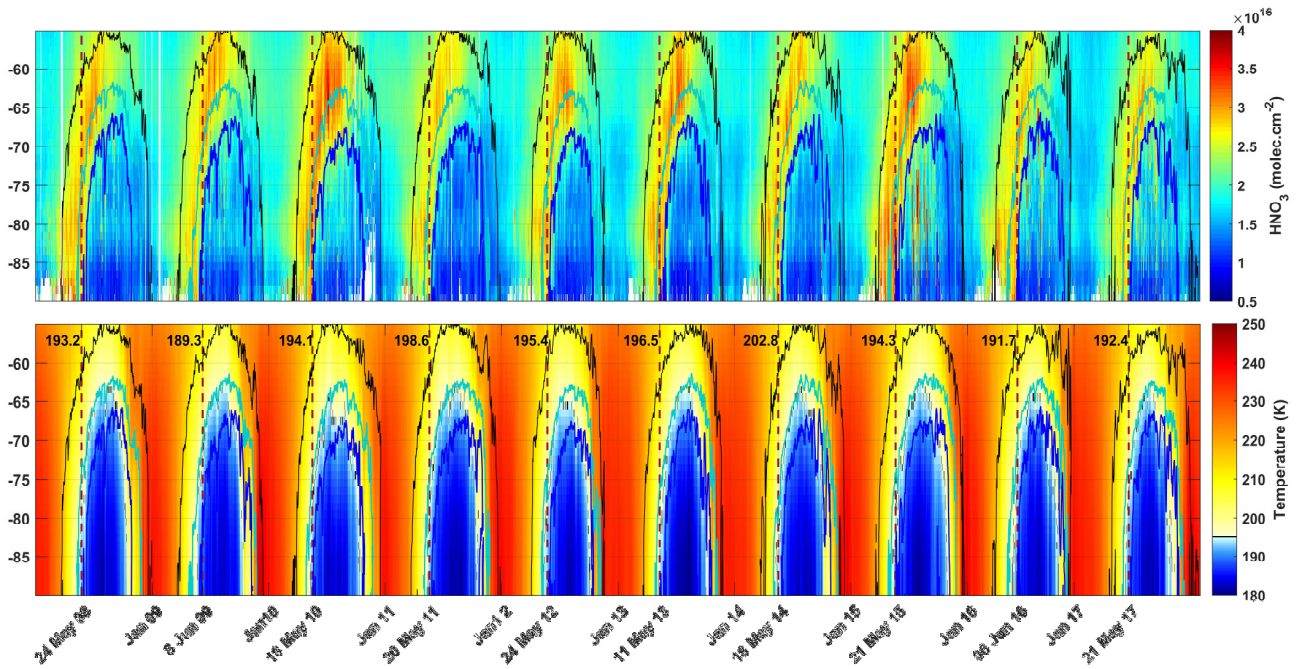
548

549

550

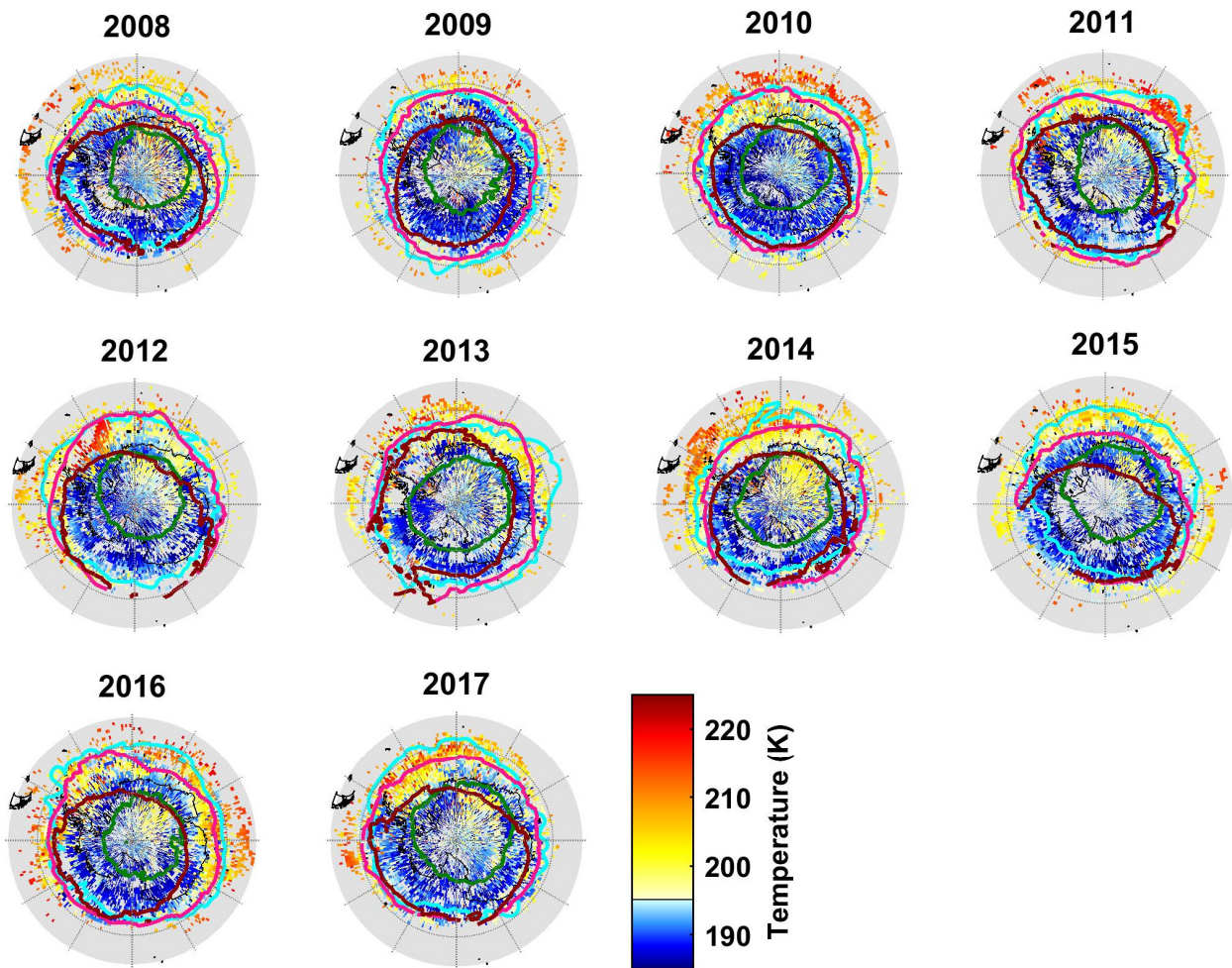


551  
552 **Figure 5.** Zonal distributions of (a)  $\text{HNO}_3$  total columns (in  $\text{molec.cm}^{-2}$ ) from IASI and (b) temperatures at 50  
553 hPa from ERA Interim (in K) in the  $55^{\circ}$  S to  $90^{\circ}$  S geographical latitude band and averaged over the years 2008  
554 – 2017. Three isocontours for the climatological (2008–2017) and zonally averaged PV of -5 (black), -8 (cyan)  
555 and -10 ( $\times 10^{-5} \text{ K.m}^2.\text{kg}^{-1}.\text{s}^{-1}$ ) at 530 K, as well as the isocontours for the 195 K climatological (2008–2017)  
556 zonally averaged temperature (pink) and for the averaged 194.2 K drop temperature (purple) at 50 hPa are  
557 superimposed. The vertical grey dashed lines mark the earliest and latest dates for the averaged drop temperature  
558 in the 10-year IASI record and the red one indicates the average date for the drop temperatures calculated in the  
559 area delimited by the  $-10 \times 10^{-5} \text{ K.m}^2.\text{kg}^{-1}.\text{s}^{-1}$  PV contour.  
560  
561



562  
563 **Figure 6.** Zonally averaged distributions of (top) HNO<sub>3</sub> total columns (in molec.cm<sup>-2</sup>) from IASI and (bottom)  
564 temperatures at 50 hPa from ERA Interim (in K). The geographical latitude range is from 55° to 90° south and  
565 the isocontours are PVs of -5 (black), -8 (cyan) and -10 (blue) ( $\times 10^{-5}$  K.m<sup>2</sup>.kg<sup>-1</sup>.s<sup>-1</sup> at 530 K). The vertical red  
566 dashed lines correspond to the second derivative minima each year in the area delimited by a  $-10 \times 10^{-5}$  K.m<sup>2</sup>.kg<sup>-1</sup>.s<sup>-1</sup> PV contour.  
567

568  
569  
570



571  
 572 **Figure 7.** Spatial distribution ( $1^\circ \times 1^\circ$ ) of the drop temperature at 50 hPa (K) (calculated from the total  $\text{HNO}_3$   
 573 second derivative minima) for each year of IASI (2008–2017), in a region defined by a PV of  $-8 \times 10^{-5} \text{ K.m}^2.\text{kg}^{-1}.\text{s}^{-1}$ .  
 574 The isocontours of  $-10 \times 10^{-5} \text{ K.m}^2.\text{kg}^{-1}.\text{s}^{-1}$  at 530 K for the averaged PV (in green) and the minimum PV (in  
 575 cyan) encountered over the period 10 May–15 July for each year and the isocontours of 195 K at 50 hPa for the  
 576 averaged (in red) and the minimum (in pink) temperatures over the same period are represented.  
 577  
 578  
 579  
 580  
 581  
 582  
 583  
 584  
 585  
 586  
 587  
 588  
 589

590

## References

591

592

593

594

595

596

597

598

599

600

601

602

603

604

605

606

607

608

609

610

611

612

613

614

615

616

617

618

619

620

621

622

623

624

625

626

627

628

629

630

631

632

633

634

635

636

637

638

639

640

641

642

643

644

645

646

647

Braun, M., Groß, J.-U., Woiwode, W., Johansson, S., Höpfner, M., Friedl-Vallon, F., Oelhaf, H., Preusse, P., Ungermann, J., Sinnhuber, B.-M., Ziereis, H., and Braesicke, P.: Nitrification of the lowermost stratosphere during the exceptionally cold Arctic winter 2015/16, *Atmospheric Chemistry and Physics Discussions*, <https://doi.org/10.5194/acp-2019-108>, 2019.

Carslaw, K. S., Luo, B. P., and Peter, T.: An analytical expression for the composition of aqueous  $\{\text{HNO}_3\text{-H}_2\text{SO}_4\text{-H}_2\text{O}\}$  stratospheric aerosols including gas phase removal of  $\text{HNO}_3$ , *Geophys. Res. Lett.*, 22, 1877–1880, <https://doi.org/10.1029/95GL01668>, 1995.

Carslaw, K. S., Wirth, M., Tsias, A., Luo, B. P., Dörnbrack, A., Leutbecher, M., Volkert, H., Renger, W., Bacmeister, J. T., Reimer, E., and Peter, T.: Increased stratospheric ozone depletion due to mountain-induced atmospheric waves, *Nature*, 391, 675–678, <https://doi.org/10.1038/35589>, 1998.

Clerbaux, C., Boynard, A., Clarisse, L., George, M., Hadji-Lazaro, J., Herbin, H., Hurtmans, D., Pommier, M., Razavi, A., Turquety, S., Wespes, C., and Coheur, P.-F.: Monitoring of atmospheric composition using the thermal infrared IASI/MetOp sounder, *Atmospheric Chemistry and Physics*, 9, 6041–6054, <https://doi.org/10.5194/acp-9-6041-2009>, 2009.

de Laat, A. T. J. and van Weele, M.: The 2010 Antarctic ozone hole: Observed reduction in ozone destruction by minor sudden stratospheric warmings, *Scientific Reports*, 1, 38, <https://doi.org/10.1038/srep00038>, 2011.

de Zafra, R. and Smyshlyaev, S. P.: On the formation of  $\text{HNO}_3$  in the Antarctic mid to upper stratosphere in winter, *Journal of Geophysical Research*, 106, 23 115, <https://doi.org/10.1029/2000JD000314>, 2001.

Groß, J. U., Engel, I., Borrman, S., Frey, W., Günther, G., Hoyle, C. R., Kivi, R., Luo, B. P., Molleker, S., Peter, T., Pitts, M. C., Schlager, H., Stiller, G., Vömel, H., Walker, K. a., and Müller, R.: Nitric acid trihydrate nucleation and denitrification in the Arctic stratosphere, *Atmospheric Chemistry and Physics*, 14, 1055–1073, <https://doi.org/10.5194/acp-14-1055-2014>, 2014.

Hanson, D. and Mauersberger, K.: Laboratory studies of the nitric acid trihydrate: Implications for the south polar stratosphere, *Geophysical Research Letters*, 15, 855–858, <https://doi.org/10.1029/GL015i008p00855>, 1988.

Harris, N. R. P., Lehmann, R., Rex, M., and von der Gathen, P.: A closer look at Arctic ozone loss and polar stratospheric clouds, *Atmospheric Chemistry and Physics*, 10, 8499–8510, <https://doi.org/10.5194/acp-10-8499-2010>, 2010.

Hilton, F., Armante, R., August, T., Barnet, C., Bouchard, A., Camy-Peyret, C., Capelle, V., Clarisse, L., Clerbaux, C., Coheur, P.-F., Collard, A., Crevoisier, C., Dufour, G., Edwards, D., Fajian, F., Fourrié, N., Gambacorta, A., Goldberg, M., Guidard, V., Hurtmans, D., Illingworth, S., Jacquinot-Husson, N., Kerzenmacher, T., Klaes, D., Lavanant, L., Masiello, G., Matricardi, M., McNally, A., Newman, S., Pavelin, E., Payan, S., Péquignot, E., Peyridieu, S., Phulpin, T., Remedios, J., Schlüssel, P., Serio, C., Strow, L., Stubenrauch, C., Taylor, J., Tobin, D., Wolf, W., and Zhou, D.: Hyperspectral Earth Observation from IASI: Five Years of Accomplishments, *Bulletin of the American Meteorological Society*, 93, 347–370, <https://doi.org/10.1175/BAMS-D-11-00027.1>, 2012.

Hoffmann, L., Spang, R., Orr, A., Alexander, M. J., Holt, L. A., and Stein, O.: A decadal satellite record of gravity wave activity in the lower stratosphere to study polar stratospheric cloud formation, *Atmospheric Chemistry and Physics*, 17, 2901–2920, <https://doi.org/10.5194/acp-17-2901-2017>, 2017.

Höpfner, M., Luo, B. P., Massoli, P., Cairo, F., Spang, R., Snels, M., Di Donfrancesco, G., Stiller, G., von Clarmann, T., Fischer, H., and Biermann, U.: Spectroscopic evidence for NAT, STS, and ice in MIPAS infrared limb emission measurements of polar stratospheric clouds, *Atmospheric Chemistry and Physics*, 6, 1201–1219, <https://doi.org/10.5194/acp-6-1201-2006>, 2006.

Höpfner, M., Pitts, M. C., and Poole, L. R.: Comparison between CALIPSO and MIPAS observations of polar stratospheric clouds, *Journal of Geophysical Research Atmospheres*, 114, 1–15, <https://doi.org/10.1029/2009JDO12114>, 2009.

Hoyle, C. R., Engel, I., Luo, B. P., Pitts, M. C., Poole, L. R., Groß, J. U., and Peter, T.: Heterogeneous formation of polar stratospheric clouds- Part 1: Nucleation of nitric acid trihydrate (NAT), *Atmospheric Chemistry and Physics*, 13, 9577–9595, <https://doi.org/10.5194/acp-13-9577-2013>, 2013.

648  
649  
650  
651  
652  
653  
654  
655  
656  
657  
658  
659  
660  
661  
662  
663  
664  
665  
666  
667  
668  
669  
670  
671  
672  
673  
674  
675  
676  
677  
678  
679  
680  
681  
682  
683  
684  
685  
686  
687  
688  
689  
690  
691  
692  
693  
694  
695  
696  
697  
698  
699  
700  
701  
702  
703

Hurtmans, D., Coheur, P.-F., Wesp, C., Clarisse, L., Scharf, O., Clerbaux, C., Hadji-Lazaro, J., George, M., and Turquety, S.: FORLI radiative transfer and retrieval code for IASI, *Journal of Quantitative Spectroscopy and Radiative Transfer*, 113, 1391–1408, <https://doi.org/10.1016/j.jqsrt.2012.02.036>, 2012.

James, A. D., Brooke, J. S. A., Mangan, T. P., Whale, T. F., Plane, J. M. C., and Murray, B. J.: Nucleation of nitric acid hydrates in polar stratospheric clouds by meteoric material, *Atmospheric Chemistry and Physics*, 18, 4519–4531, <https://doi.org/10.5194/acp-18-4519-2018>, 2018.

Keys, J. G., Johnston, P. V., Blatherwick, R. D., and Murcay, F. J.: Evidence for heterogeneous reactions in the Antarctic autumn stratosphere, *Nature*, 361, 49–51, <https://doi.org/10.1038/361049a0>, 1993.

Klekociuk, A., Tully, M., Alexander, S., Dargaville, R., Deschamps, L., Fraser, P., Gies, H., Henderson, S., Javorniczky, J., Krummel, P., Petelina, S., Shanklin, J., Siddaway, J., and Stone, K.: The Antarctic ozone hole during 2010, *Australian Meteorological and Oceanographic Journal*, 61, 253–267, <https://doi.org/10.22499/2.6104.006>, 2011.

Koop, T., Luo, B., Tsias, A., and Peter, T.: Water activity as the determinant for homogeneous ice nucleation in aqueous solutions, *Nature*, 406, 611–614, <https://doi.org/10.1038/35020537>, 2000.

Lambert, A., Santee, M. L., Wu, D. L., and Chae, J. H.: A-train CALIOP and MLS observations of early winter Antarctic polar stratospheric clouds and nitric acid in 2008, *Atmospheric Chemistry and Physics*, 12, 2899–2931, <https://doi.org/10.5194/acp-12-2899-2012>, 2012.

Lambert, A., Santee, M. L., and Livesey, N. J.: Interannual variations of early winter Antarctic polar stratospheric cloud formation and nitric acid observed by CALIOP and MLS, *Atmospheric Chemistry and Physics*, 16, 15 219–15 246, <https://doi.org/10.5194/acp-16-15219-2016>, 2016.

Lambert, A. and Santee, M. L.: Accuracy and precision of polar lower stratospheric temperatures from reanalyses evaluated from A-Train CALIOP and MLS, COSMIC GPS RO, and the equilibrium thermodynamics of supercooled ternary solutions and ice clouds, *Atmospheric Chemistry and Physics*, 18, 1945–1975, <https://doi.org/10.5194/acp-18-1945-2018>, 2018.

Lowe, D. and MacKenzie, A. R.: Polar stratospheric cloud microphysics and chemistry, *Journal of Atmospheric and Solar-Terrestrial Physics*, 70, 13–40, <https://doi.org/10.1016/j.jastp.2007.09.011>, 2008.

Molleker, S., Borrman, S., Schlager, H., Luo, B., Frey, W., Klingebiel, M., Weigel, R., Ebert, M., Mitev, V., Matthey, R., Woiwode, W., Oelhaf, H., Dörnbrack, A., Stratmann, G., Grooß, J.-U., Günther, G., Vogel, B., Müller, R., Krämer, M., Meyer, J., and Cairo, F.: Microphysical properties of synoptic-scale polar stratospheric clouds: in situ measurements of unexpectedly large HNO<sub>3</sub>-containing particles in the Arctic vortex, *Atmospheric Chemistry and Physics*, 14, 10 785–10 801, <https://doi.org/10.5194/acp-14-10785-2014>, 2014.

Murphy, D. M. and Koop, T.: Review of the vapour pressures of ice and supercooled water for atmospheric applications, *Quarterly Journal of the Royal Meteorological Society*, 131, 1539–1565, <https://doi.org/10.1256/qj.04.94>, 2005.

Peter, T.: Microphysics and heterogeneous chemistry of polar stratospheric clouds, *Annual Review of Physical Chemistry*, 48, 785–822, <https://doi.org/10.1146/annurev.physchem.48.1.785>, 1997.

Peter, T. and Grooß, J.-U.: Chapter 4. Polar Stratospheric Clouds and Sulfate Aerosol Particles: Microphysics, Denitrification and Heterogeneous Chemistry, in: *Stratospheric Ozone Depletion and Climate Change*, pp. 108–144, Royal Society of Chemistry, <https://doi.org/10.1039/9781849733182-00108>, 2012.

Piccolo, C. and Dudhia, A.: Precision validation of MIPAS-Envisat products, *Atmospheric Chemistry and Physics*, 7, 1915–1923, <https://doi.org/10.5194/acp-7-1915-2007>, 2007.

Pitts, M. C., Poole, L. R., Dörnbrack, A., and Thomason, L. W.: The 2009–2010 Arctic polar stratospheric cloud season: A CALIPSO perspective, *Atmospheric Chemistry and Physics*, 11, 2161–2177, <https://doi.org/10.5194/acp-11-2161-2011>, 2011.

704 Pitts, M. C., Poole, L. R., Lambert, A., and Thomason, L.W.: An assessment of CALIOP polar stratospheric cloud  
705 composition classification, *Atmospheric Chemistry and Physics*, 13, 2975–2988, <https://doi.org/10.5194/acp-13-2975-2013>,  
706 2013.

707

708 Pitts, M. C., Poole, L. R., and Gonzalez, R.: Polar stratospheric cloud climatology based on CALIPSO spaceborne lidar  
709 measurements from 2006 to 2017, *Atmospheric Chemistry and Physics*, 18, 10 881–10 913, <https://doi.org/10.5194/acp-18-10881-2018>, 2018.

710

711 Rodgers, C. D.: *Inverse Methods for Atmospheric Sounding - Theory and Practice*, vol. 2 of Series on Atmospheric Oceanic  
712 and Planetary Physics, World Scientific Publishing Co. Pte. Ltd., <https://doi.org/10.1142/9789812813718>, 2000.

713

714 Roscoe, H. K., Feng, W., Chipperfield, M. P., Trainic, M., and Shuckburgh, E. F.: The existence of the edge region of the  
715 Antarctic stratospheric vortex, *J. Geophys. Res.*, 117, D04301, doi:10.1029/2011JD015940, 2012.

716

717 Ronsmans, G., Langerock, B., Wespes, C., Hannigan, J. W., Hase, F., Kerzenmacher, T., Mahieu, E., Schneider, M., Smale,  
718 D., Hurtmans, D., De Mazière, M., Clerbaux, C., and Coheur, P.-F.: First characterization and validation of FORLI-HNO<sub>3</sub>  
719 vertical profiles retrieved from IASI/Metop, *Atmospheric Measurement Techniques*, 9, 4783–4801,  
720 <https://doi.org/10.5194/amt-9-4783-2016>, 2016.

721

722

723 Ronsmans, G., Wespes, C., Hurtmans, D., Clerbaux, C., and Coheur, P.-F.: Spatio-temporal variations of nitric acid total  
724 columns from 9 years of IASI measurements – a driver study, *Atmospheric Chemistry and Physics*, 18, 4403–4423,  
725 <https://doi.org/10.5194/acp-18-4403-2018>, 2018.

726

727 Santee, M. L., Manney, G. L., Froidevaux, L., Read, W. G., and Waters, J. W.: Six years of UARS Microwave Limb Sounder  
728 HNO<sub>3</sub> observations : Seasonal, interhemispheric, and interannual variations in the lower stratosphere, *Journal of Geophysical  
729 Research*, 104, 8225–8246, <https://doi.org/10.1029/1998JD100089>, 1999.

730

731 Santee, M. L., Lambert, A., Read, W. G., Livesey, N. J., Cofield, R. E., Cuddy, D. T., Daffer, W. H., Drouin, B. J., Froidevaux,  
732 L., Fuller, R. A., Jarnot, R. F., Knosp, B. W., Manney, G. L., Perun, V. S., Snyder, W. V., Stek, P. C., Thurstans, R. P.,  
733 Wagner, P. A., Waters, J. W., Muscari, G., de Zafra, R. L., Dibb, J. E., Fahey, D. W., Popp, P. J., Marcy, T. P., Jucks, K. W.,  
734 Toon, G. C., Stachnik, R. A., Bernath, P. F., Boone, C. D., Walker, K. A., Urban, J., and Murtagh, D.: Validation of the Aura  
735 Microwave Limb Sounder HNO<sub>3</sub> measurements, *Journal of Geophysical Research*, 112, 1–22,  
736 <https://doi.org/10.1029/2007JD008721>, 2007.

737

738 Schreiner, J., Voigt, C., Weisser, C., Kohlmann, A., Mauersberger, K., Deshler, T., Kröger, C., Rosen, J., Kjome, N., Larsen,  
739 N., Adriani, A., Cairo, F., Donfrancesco, G. D., Ovarlez, J., Ovarlez, H., and Dörnbrack, A.: Chemical, microphysical, and  
740 optical properties of polar stratospheric clouds, *Journal of Geophysical Research*, 108, 1–10,  
741 <https://doi.org/10.1029/2001JD000825>, 2003.

742

743 Sheese, P. E., Walker, K. A., Boone, C. D., Bernath, P. F., Froidevaux, L., Funke, B., Raspollini, P., and von Clarmann, T.:  
744 ACE-FTS ozone, water vapour, nitrous oxide, nitric acid, and carbon monoxide profile comparisons with MIPAS and MLS,  
745 *Journal of Quantitative Spectroscopy and Radiative Transfer*, 186, 63–80, <https://doi.org/10.1016/j.jqsrt.2016.06.026>, 2017.

746

747 Snels, M., Scoccione, A., Liberto, L. D., Colao, F., Pitts, M., Poole, L., Deshler, T., Cairo, F., Cagnazzo, C., and Fierli, F.:  
748 Comparison of Antarctic polar stratospheric cloud observations by ground-based and space-borne lidar and relevance for  
749 chemistry–climate models, *Atmospheric Chemistry and Physics*, 19, 955–972, <https://doi.org/10.5194/acp-19-955-2019>,  
750 2019.

751

752 Solomon, S.: Stratospheric ozone depletion: A review of concepts and history, *Reviews of Geophysics*, 37, 275–316,  
753 <https://doi.org/10.1029/1999RG900008>, 1999.

754

755 Spang, R., Hoffmann, L., Höpfner, M., Giessbach, S., Müller, R., Pitts, M. C., Orr, A. M. W., and Riese, M.: A multi-  
756 wavelength classification method for polar stratospheric cloud types using infrared limb spectra, *Atmospheric Measurement  
757 Techniques*, 9, 3619–3639, <https://doi.org/10.5194/amt-9-3619-2016>, 2016.

758

759 Spang, R., Hoffmann, L., Müller, R., Groß, J.-U., Tritscher, I., Höpfner, M., Pitts, M., Orr, A., and Riese, M.: A climatology  
760 of polar stratospheric cloud composition between 2002 and 2012 based on MIPAS/Envisat observations, *Atmospheric  
761 Chemistry and Physics*, 18, 5089–5113, <https://doi.org/10.5194/acp-18-5089-2018>, 2018.

762  
763 Toon, O. B., Hamill, P., Turco, R. P., and Pinto, J.: Condensation of HNO<sub>3</sub> and HCl in the winter polar stratospheres,  
764 Geophysical Research Letters, 13, 1284–1287, <https://doi.org/10.1029/GL013i012p01284>, 1986.  
765  
766 Tritscher, I., Pitts, M. C., Poole, L. R., Alexander, S. P., Cairo, F., Chipperfield, M. P., et al.: Polar stratospheric clouds:  
767 Satellite observations, processes, and role in ozone depletion, Reviews of Geophysics, 59, e2020RG000702,  
768 <https://doi.org/10.1029/2020RG000702>.  
769  
770 Urban, J., Pommier, M., Murtagh, D. P., Santee, M. L., and Orsolini, Y. J.: Nitric acid in the stratosphere based on Odin  
771 observations from 2001 to 2009 – Part 1: A global climatology, Atmospheric Chemistry and Physics, 9, 7031–7044,  
772 <https://doi.org/10.5194/acp-9-7031-2009>, 2009.  
773  
774 Voigt, C., Schreiner, J., Kohlmann, A., Zink, P., Mauersberger, K., Larsen, N., Deshler, T., Kro, C., Rosen, J., Adriani, A.,  
775 Cairo, F., Donfrancesco, G. D., Viterbini, M., Ovarlez, J., Ovarlez, H., and David, C.: Nitric Acid Trihydrate (NAT) in Polar  
776 Stratospheric Clouds, Science, 290, 1756–1758, <https://doi.org/10.1126/science.290.5497.1756>, 2000.  
777  
778 Voigt, C., Larsen, N., Deshler, T., et al.: In situ mountainwave polar stratospheric cloud measurements: Implications for nitric  
779 acid trihydrate formation, J. Geophys. Res., 108(D5), doi:10.1029/2001JD001185, 2003.  
780  
781 Voigt, C., Schlager, H., Luo, B. P., Dörnbrack, A., Roiger, A., Stock, P., Curtius, J., Vössing, H., Borrmann, S., Davies, S.,  
782 Konopka, P., Schiller, C., Shur, G., and Peter, T.: Nitric Acid Trihydrate (NAT) formation at low NAT supersaturation in  
783 Polar Stratospheric Clouds (PSCs), Atmospheric Chemistry and Physics, 5, 1371–1380, <https://doi.org/10.5194/acp-5-1371-2005>, 2005.  
784  
785 von König, M.: Using gas-phase nitric acid as an indicator of PSC composition, Journal of Geophysical Research, 107,  
786 <https://doi.org/10.1029/2001jd001041>, 2002.  
787  
788 Wang, X. and Michelangeli, D. V.: A review of polar stratospheric cloud formation, China Particuology, 4, 261–271,  
789 [https://doi.org/10.1016/S1672-2515\(07\)60275-9](https://doi.org/10.1016/S1672-2515(07)60275-9), 2006.  
790  
791 Wegner, T., Groß, J.-U., von Hobe, M., Stroh, F., Sumin'ska-Ebersoldt, O., Volk, C. M., Hösen, E., Mitev, V., Shur, G.,  
792 and Müller, R.: Heterogeneous chlorine activation on stratospheric aerosols and clouds in the Arctic polar vortex,  
793 Atmospheric Chemistry and Physics, 12, 11 095–11 106, <https://doi.org/10.5194/acp-12-11095-2012>, 2012.  
794  
795 Wespes, C., Hurtmans, D., Clerbaux, C., and Coheur, P.-F.: O<sub>3</sub> variability in the troposphere as observed by IASI over 2008–  
796 2016: Contribution of atmospheric chemistry and dynamics, Journal of Geophysical Research: Atmospheres, 122, 2429–  
797 2451, <https://doi.org/10.1002/2016JD025875>, <http://doi.wiley.com/10.1002/2016JD025875>, 2017.  
798  
799 800 WMO: Scientific Assessment of Ozone Depletion: 2014, Global Ozone Research and Monitoring Project – Report No. 55,  
801 World Meteorological Organization, Geneva, Switzerland, 2014.  
802  
803 Zhu, Y., Toon, O. B., Lambert, A., Kinnison, D. E., Brakebusch, M., Bardeen, C. G., Mills, M. J., and English, J. M.:  
804 Development of a Polar Stratospheric Cloud Model within the Community Earth System Model using constraints on Type I  
805 PSCs from the 2010–2011 Arctic winter, Journal of Advances in Modeling Earth Systems, 7, 551–585,  
806 <https://doi.org/10.1002/2015ms000427>, 2015.  
807  
808 Zondlo, M. A., P. K. Hudson, A. J. Prenni, and M. A. Tolbert: Chemistry and microphysics of polar stratospheric clouds and  
809 cirrus clouds, Annu. Rev. Phys. Chem., 51, 473–499, 2000.